




Article

Application of Scanning Precession Electron Diffraction in the Transmission Electron Microscope to the Characterization of Deformation in Wadsleyite and Ringwoodite

Billy C. Nzogang ¹ , Simon Thilliez ¹, Alexandre Mussi ¹, Takaaki Kawazoe ^{2,3}, Nobuyoshi Miyajima ² , Jérémie Bouquerel ¹ and Patrick Cordier ^{1,*} 

¹ CNRS, INRA, ENSCL, UMR 8207-UMET-Unité Matériaux et Transformations, University of Lille, F-59000 Lille, France; bc.nzogang@etudiant.univ-lille1.fr (B.C.N.); simon.thilliez@gmail.com (S.T.); alexandre.mussi@univ-lille1.fr (A.M.); jeremie.bouquerel@univ-lille1.fr (J.B.)

² Bayerisches Geoinstitut, University of Bayreuth, D-95440 Bayreuth, Germany; kawazoe@hiroshima-u.ac.jp (T.K.); nobuyoshi.miyajima@uni-bayreuth.de (N.M.)

³ Department of Earth and Planetary Systems Science, Hiroshima University, Higashi-Hiroshima 739-8526, Japan

* Correspondence: patrick.cordier@univ-lille1.fr; Tel.: +33-320-434-34341

Received: 19 March 2018; Accepted: 10 April 2018; Published: 12 April 2018



Abstract: The mantle transition zone represents an important layer in the interior of the Earth that is characterized by phase transformations of olivine polymorphs. Constraining the rheology difference between wadsleyite and ringwoodite is important in determining the viscosity contrast at a depth of 520 km. In this study, we perform a post-mortem by transmission electron microscopy of a wadsleyite + ringwoodite aggregate, deformed at high-pressure and high-temperature, in a deformation-DIA apparatus. From orientation maps acquired by scanning precession electron diffraction, we calculate local misorientations and misorientation-gradients, which are used as a proxy of plastic strain. We show that at 17.3 GPa, 1700 K, the plastic responses of wadsleyite and ringwoodite are comparable, although recovery by subgrain boundary migration is more easily activated in wadsleyite.

Keywords: mantle transition zone; wadsleyite; ringwoodite; plastic deformation; transmission electron microscopy; scanning precession electron diffraction

1. Introduction

The Earth's mantle is divided into an upper and a lower part, separated by a transition zone (TZ) at a depth of between 520 km and 670 km. The TZ is characterized by phase transitions between polymorphs of olivine: wadsleyite and ringwoodite. The viscosity of the TZ is still a matter of debate. Some studies propose that it represents a weak layer [1,2] although slab stagnation may suggest the opposite [3]. A way of answering this question is to determine experimentally the rheology of the key phases of the TZ: wadsleyite and ringwoodite. Such experiments are very challenging, due to the P, T conditions which prevail in the TZ; however, recent technological developments have made such experiments possible. Two apparatuses can presently perform deformation experiments in the P, T condition of the TZ: the rotational Drickamer apparatus [4], and the D-DIA apparatus [5]. Using these devices, several studies have addressed the rheology of wadsleyite (e.g., [6,7]) and ringwoodite [8,9], including the one describing the sample investigated here [10]. In these experiments, rheological data are obtained by coupling deformation apparatuses with synchrotron X-ray beams. The total plastic strain is usually inferred from X-ray radiography, whereas stress is deduced from

lattice strain measurements from Bragg peaks displacements. The limited availability of synchrotron beamline access represents a strong limitation associated with such investigations. In the present study, we investigate an alternative approach based on the investigation and post-mortem, by transmission electron microscopy (TEM), of samples deformed at high-pressure. Not being performed in situ, our approach cannot be seen as a substitute for synchrotron studies (for instance, in giving access to stress-strain relationships). It can, however, complement in situ experiments and allow exploiting high-pressure deformation experiments to be performed off-line.

Deformed crystals contain defect microstructures which represent a valuable source of information about their mechanical properties. In this study, these defects and dislocations will not be characterized individually (as is commonly done at the TEM; see for instance a preliminary study of this sample in [10]). Dislocations introduce a long-range strain field in their surrounding materials. Each dislocation gives rise to a small increment of misorientation. This effect has been known and used for a long time, since undulatory extinction represents a common criterion for intragranular plasticity without recovery in optical microscopy. With the advent of automated orientation mapping by electron backscatter diffraction (EBSD) in the scanning electron microscope (SEM), the measurement of intragranular misorientation has been used as a proxy for plastic strain [11,12], with applications for severely deformed materials [13,14]. Such measurements are now possible in the TEM with a very high spatial resolution, and we have demonstrated recently the capability of the technique in providing information about deformation mechanisms in a bridgmanite and ferropericlasite aggregate deformed at high-pressure and high-temperature [14].

Here we apply a technique called scanning precession electron diffraction (SPED) to the characterization of a sample deformed at 17.3 GPa and 1700 K, which contains both wadsleyite and ringwoodite. This sample represents a unique opportunity to gain information on the relative strength of the two phases, since they bore exactly the same deformation conditions.

2. Materials and Methods

2.1. Sample M1219: Synthesis and Deformation

Deformation of the sample characterized in this study (reference M1219) has been described in [10]. The main information is summarized here. Polycrystalline ringwoodite was synthesized from an olivine (San Carlos origin with composition $(\text{Mg}_{0.9}\text{Fe}_{0.1})_2\text{SiO}_4$) aggregate while increasing temperature to 1700 K at ~17–18 GPa in the D-DIA apparatus at the BL04B1 beamline of SPring-8. The sample was axially deformed with stress-strain measurements by X-ray diffraction and radiography respectively. Ringwoodite partially transformed to wadsleyite after a strain of 14.8% during deformation at 17.3 GPa and 1700 K. The wadsleyite + ringwoodite aggregate was further deformed to a strain of 24.9%. Stresses of coexisting wadsleyite and ringwoodite were not determined because X-ray diffraction peaks of ringwoodite (e.g., 220, 311 and 400) overlaps with those of wadsleyite (e.g., 040 + 200, 141 and 240), due to similarity between their crystal structures.

2.2. TEM Characterization

For the TEM investigation, sample foils were cut from the deformed samples using a dual beam focused ion (FIB) milling machine with Ga ion and electron beams (FEI (Hillsboro, OR, United States), Scios at the Bayerisches Geoinstitut, Bayreuth, Germany). TEM investigations were performed at the University of Lille with a FEI® Tecnai G²20Twin microscope (FEI, Hillsboro, OR United States), operating at 200 kV, and with a Philips CM30 microscope operating (now FEI, Hillsboro, OR, United States) at 300 kV; both were equipped with a LaB₆ filament and were using a double tilt sample-holder.

Orientation maps were acquired with a step size of 5 nm, using SPED in the TEM with the ASTAR™ tool from NanoMEGAS (Forest, Belgium) [15]. The TEM is set in micro-beam mode (spot size 4 nm), and the incident electron beam, which is focused on the sample, is scanned over the area thanks to a dedicated hardware control system composed of TEM deflecting coils. In this mode, where

the sample is illuminated by a convergent beam, the diffraction pattern consists of discs. Using the smallest condenser aperture (50 μm) the diffraction patterns are made of very small, spot-like discs, and can be indexed as spot patterns. The individual exposure time at each location is 10 ms. In this study, we used precession illumination (with a precession angle of 0.5°) in the TEM, which allows many more reflections to be seen in the diffraction pattern with intensities closer to the kinematical diffraction conditions. Diffraction patterns are collected with an external Stingray CCD camera (Allied Vision Technologies GmbH, Stadtroda, Germany) that points on the TEM phosphorous screen, and stored in the computer memory for further indexation and post processing. The diffraction patterns were collected as 144×144 pixel images, at a camera length of 89 mm. In the ASTAR system, electron diffraction spot patterns are indexed (providing the local crystal orientations) by comparing individually obtained patterns via cross-correlation matching techniques with pre-calculated electron diffraction templates generated every 0.5° (orientation resolution). For wadsleyite and ringwoodite, templates have been generated from the crystallographic data of Horiuchi and Sawamoto [16] and Hazen et al. [17] respectively. From this indexation, one obtains an orientation map which displays, with a color coding, the most probable orientation at each scanned beam position.

The quality of indexation from template matching is quantified by the image correlation index, which is calculated for every template [18]:

$$Q(i) = \frac{\sum_{j=1}^m P(x_j, y_j) T_i(x_j, y_j)}{\sqrt{\sum_{j=1}^m P^2(x_j, y_j)} \sqrt{\sum_{j=1}^m T_i^2(x_j, y_j)}} \quad (1)$$

In this expression, the diffraction pattern is represented by the intensity function $P(x, y)$, and every template i is described by the function $T_i(x, y)$. The highest Q value corresponds to the solution retained. The reliability of this solution can be quantified by the ratio of the matching indexes for the two best solutions Q_1 and Q_2 :

$$R = 100 \left(1 - \frac{Q_1}{Q_2} \right) \quad (2)$$

In reliability maps, the brighter the pixel, the more reliable the indexation proposed is. On the contrary, the darker the pixel, the less the solution is reliable. This is typically the case at grain boundaries where two solutions of co-existing grains overlap, or when for various reasons, the quality of the diffraction patterns is diminished.

In this study we use orientation maps to calculate local misorientations, as recently developed in the EBSD community (e.g., [19]). Post-processing of the orientation maps was performed using HKL Channel 5 software (Oxford Instruments, Abingdon-on-Thames, United Kingdom). As commonly used in EBSD, several quantities are calculated from the orientation maps:

The Kernel Average Misorientation (KAM) calculates the average misorientation between a pixel and its neighbors, provided that the misorientation does not exceed a predefined threshold value, e.g., 5° ; thus, the incorporation of well-defined grain boundaries is avoided. If plastic deformation results from dislocation glide and crystal lattice rotation, this approach allows quantitative evaluation of the local plastic strain gradients [20]. A kernel is a set of points of prescribed size surrounding the scan point of interest. The size of the kernel is generally prescribed to the n th nearest-neighbors. Hence this parameter is sensitive to the step size of the measurement grid.

- The Grain Orientation Spread (GOS) is the average deviation in orientation between each point in a grain and the average orientation of the grain. This approach leads to assigning the same value of the GOS to every scan point contained within a grain. The minimum area grain size is set to 100 pixels (ca. 50 nm in diameter assuming quasi-spherical grains), and the grain tolerance angle is set to 15° .
- The Grain Reference Orientation Deviation (GROD) is based on the misorientation between a reference point of that grain and the other points. The reference point can be the mean misorientation of the grain or the point of the grain where the KAM is the lowest.

- KAM, GROD and GOS approaches are complementary. GROD maps show the orientation field referenced to a fixed point, whereas KAM shows the magnitude of the gradient, which can be seen as the first derivative of the orientation field.

3. Results

The FIB thin section investigated in this study is shown on Figure 1a, with the area scanned by SPED appearing in red. It shows a large fraction of open grain boundaries, probably resulting from sample preparation. Hence we will focus on intragranular plasticity mechanisms only. During post-processing, each diffraction pattern at each point is compared to the patterns calculated for wadsleyite and ringwoodite. Phase identification is thus the first outcome of the process. The phase map is shown on Figure 1b. The main phase represented is wadsleyite, which represents 62.2% of the thin section. Wadsleyite also exhibits coarser grains. In the FIB section studies, some wadsleyite grains reach 4–6 μm , whereas grains of ringwoodite are in the range 0.6–2 μm . Figure 1c,d shows the inverse pole figures (IPF) of wadsleyite and ringwoodite respectively. One can already notice on those figures that the color is not completely uniform in each grain. This is more visible on ringwoodite. Slight color changes on the IPF are due to intragranular misorientations, resulting from the population of dislocations inside the grains, which are further analyzed below.

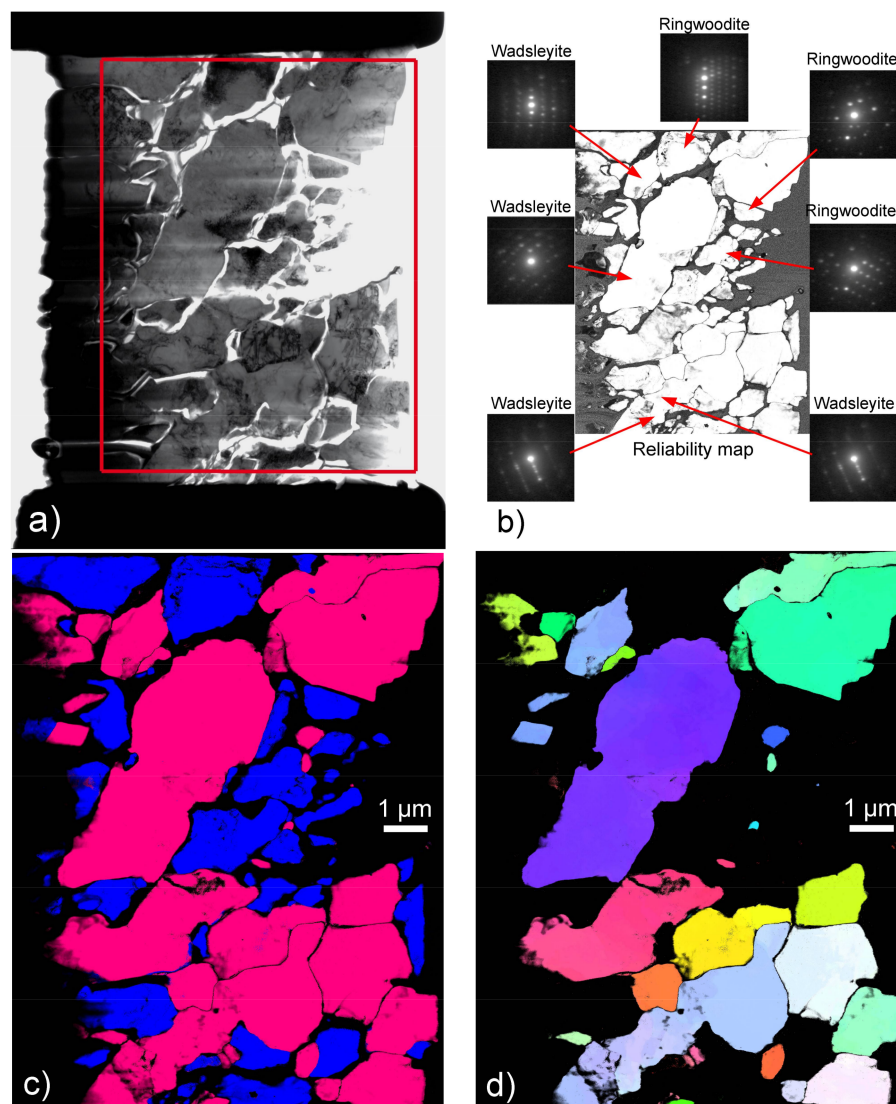


Figure 1. *Cont.*

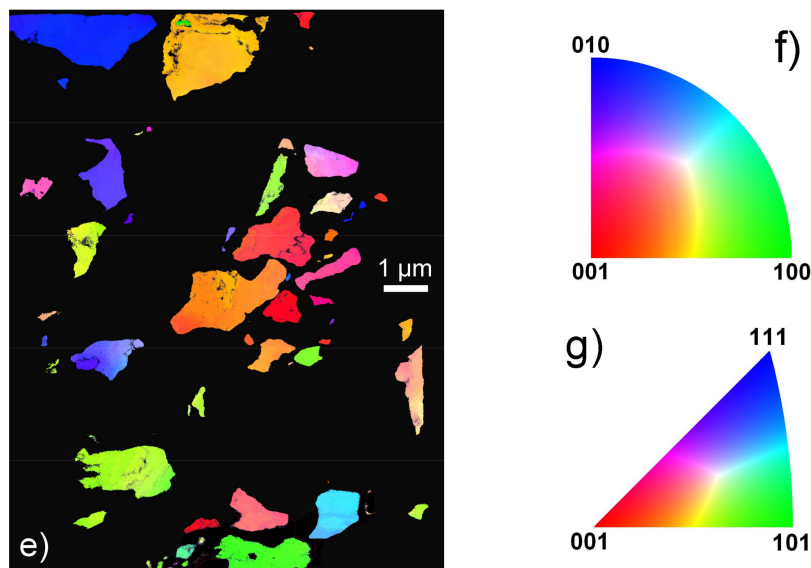


Figure 1. (a) General view of the FIB section. The compression direction is vertical; the scanned area (2200×2500 grid points) is represented by a red rectangle; (b) Reliability map (greyscale between 0 and 61) showing the quality of indexation (see text and Equation (2)), with some examples of diffraction patterns attached; (c) Phase map: wadsleyite is in red and ringwoodite is in blue; (d) Inverse pole figure (direction normal to the plane of representation) of wadsleyite (color code in f); (e) Inverse pole figure (direction normal to the plane of representation) of ringwoodite (color code in g); (f) Color code for the crystallographic orientations of the IPF in wadsleyite indexed within the $Im\bar{3}m$ space group; (g) Color code for the crystallographic orientations of the IPF in ringwoodite indexed within the $Fd\bar{3}m$ space group.

4. Discussion

To emphasize the intragranular misorientations, we applied several post-treatments of the IPF maps which are displayed in Figure 2. Figure 2a,b show the grain orientation spreadings (GOS) of wadsleyite and ringwoodite respectively. This representation gives each grain a uniform color describing the range of misorientation within the grain. One can readily see that almost all grains exhibit significant intragranular misorientations resulting from plastic deformation. It is, however, difficult to exploit this data to compare grains with different sizes, since the GOS is intrinsically grain size dependent. The GROD (Figure 2c,d) allows us to visualize how intragranular misorientations organize themselves spatially within the grains. It represents a potential means to study how plasticity transfers from one grain to another in response to grain to grain interactions (see for instance [21] for a theoretical description of such heterogeneities resulting from plastic strain): see as illustration the strain concentration in-between the two large wadsleyite grains on top of Figure 2c (white arrow). It also gives interesting clues about the processes taking place in the materials. For instance, one can see in Figure 2c a curved boundary separating two parts of a grain of wadsleyite (black arrowed on Figure 2c) which exhibit a misorientation of 6° ; this is a subgrain boundary (SGB). It is striking that, across the SGB, very distinct GROD values are observed. The part on the left is almost free of dislocations (see Figure 3, where this part has been imaged by weak-beam dark-field), whereas the part on the right exhibits a high amount of internal misorientation, as shown by the GROD. This grain is thus experiencing recovery by SGB migration, driven by the difference of stored elastic energy well highlighted by the GROD. Indeed, the center of curvature of the SGB (which gives the sense of motion) is located in the part characterized by highest GROD.

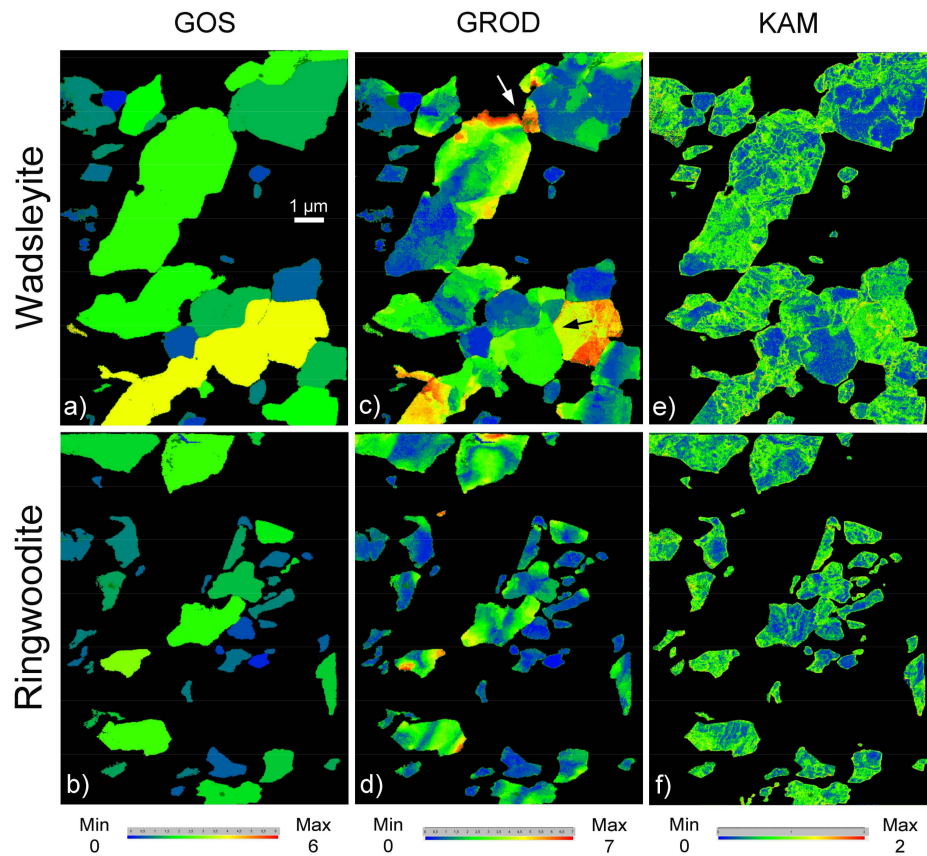


Figure 2. GOS in wadsleyite (a) and ringwoodite (grain tolerance angle 15° ; minimum area grain size 100 pixels) (b); GROD in wadsleyite (c) and ringwoodite (d); KAM (3rd nearest-neighbor) in wadsleyite (e) and ringwoodite (f).

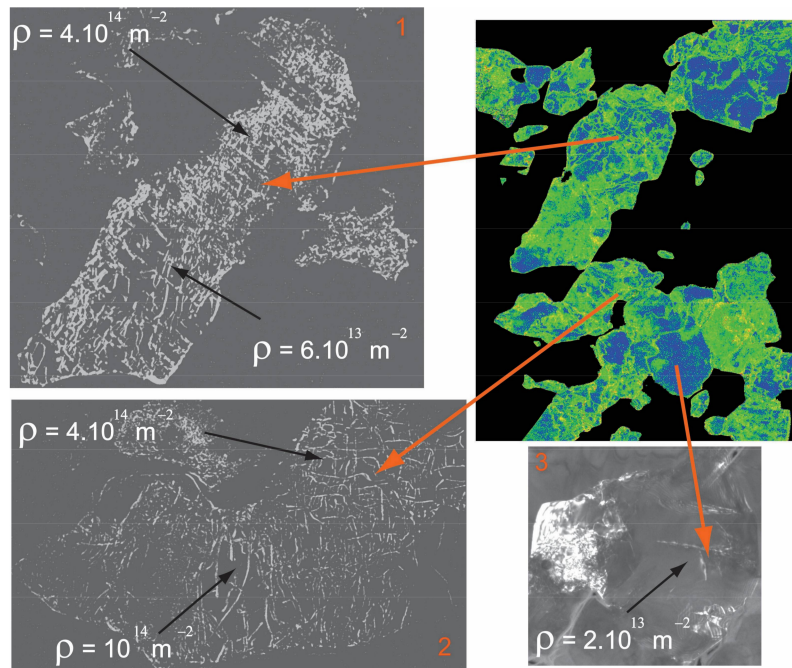


Figure 3. Weak-beam dark field images and dislocation density counts (using the method of [22]) in three grains of wadsleyite located on the KAM map of Figure 2e. Diffraction vectors: for 1, g : 440; for 2, g : 400 and for 3, g : 112.

In EBSD, the angular resolution is such that accurate measurements of geometrically necessary dislocation (GNDs) densities are now possible [23,24]. So far, applications have been mostly shown to apply to metals after severe deformation. The situation is not so favorable in SPED. The actual quantitative determination of dislocation density is indeed facing the angular resolution of SPED which, in a standard mode, is lower than in EBSD. Ghamarian et al. [13] discuss this issue and report that the minimum resolvable GND density relates to the angular resolution and to the step size:

$$\rho_{min}^{GND} = \frac{\text{angular resolution (rad)}}{\text{step size} \times \text{Burge's vector length}} \quad (3)$$

With an angular resolution of 0.5° and our step size (5 nm), the minimum dislocation density resolvable would be in the order of $3 \times 10^{15} \text{ m}^{-2}$ (in wadsleyite, which is under examination here, the Burgers vectors lengths are 0.569 nm for [100] dislocations and 0.761 nm for $\frac{1}{2}\langle 111 \rangle$ dislocations). We have conducted conventional weak-beam dark-field investigations of some grains of wadsleyite. The results are presented in Figure 3. The dislocation densities measured are in the order of 10^{14} m^{-2} , i.e., slightly below the threshold found from Equation (3). It is also worthy of mention that such measurements face the somehow artificial (or at least experimentally constrained) distinction between geometrically necessary dislocations (GNDs) and statistically stored dislocations (SSDs). In SPED, the spatial resolution is close overcoming this limitation, as shown recently by Rottmann and Hemker [25], who demonstrated that strains from individual dislocations could be mapped. Here, we decide to stay at the level of the KAM mapping. Rollett et al. [26] have shown that local gradients in orientation revealed by the KAM correlate well with plastic strain heterogeneities modeled in the framework of crystal plasticity theory.

Figure 3 shows that if the correlation between KAM maps and images of dislocations patterns is not sufficient to resolve individual dislocations and provide reliable quantitative measurements, the agreement is fair. Note that the KAM map (Figure 2e) also shows the plastic strain gradient driving the mobility of the SGB discussed above. We propose that the KAM represents a proxy of plastic strain which can be used to compare strains in different grains. In a previous study performed on an aggregate of bridgmanite and ferropericlasite [14], we avoided making such comparisons, since the two phases were undergoing very different deformation mechanisms (dense shear lamellae for bridgmanite, and homogeneous dislocation glide for ferropericlasite). Here, wadsleyite and ringwoodite both deform by dislocation glide, and exhibit very comparable dislocation microstructures. Their Burgers vectors also present comparable lengths, which should not induce any differential bias in the detection (Equation (1)). The results are presented in Figure 4. Beyond 0.8° , the KAM distributions are similar for both phases. For lower misorientations, the curves are slightly different with those of ringwoodite, exhibiting a log-normal profile (whereas the wadsleyite shows a distinct peak at 0.2°).

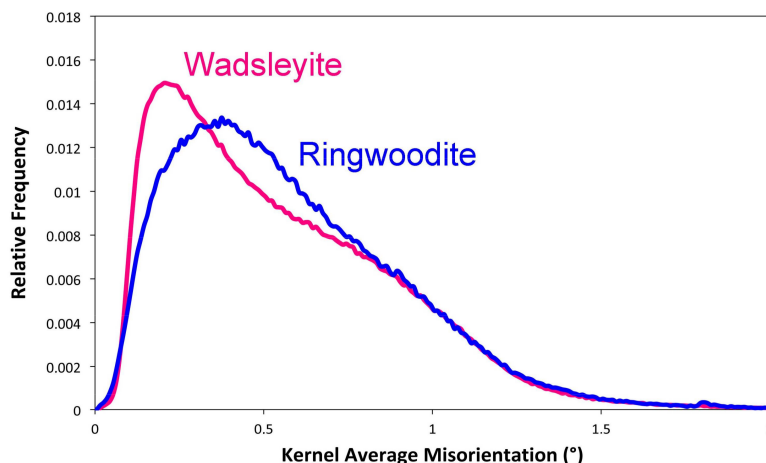


Figure 4. KAM distributions (3rd nearest-neighbor) in wadsleyite and ringwoodite.

The difference between the two minerals is illustrated in Figure 5. In Figure 5a, we show the KAM distributions samples in two regions located on both sides of the SGB already mentioned. The KAM distributions of those two regions reproduce the peaks of the global distribution. We propose that the peculiar shape of the KAM distribution of wadsleyite reflects activation of recovery driven by SGB migration. Apparently, this mechanism is not activated in ringwoodite. One might not exclude the possibility that the difference in behavior is related to the smaller grain size of ringwoodite grains. However, we raise the possibility that this is due to the fact that ringwoodite, being cubic, activates many slip systems with non-perpendicular Burgers vectors, which give rise to profuse interactions (junctions), leading to a dislocation storage which is less favorable to the formation and migration of SGBs.

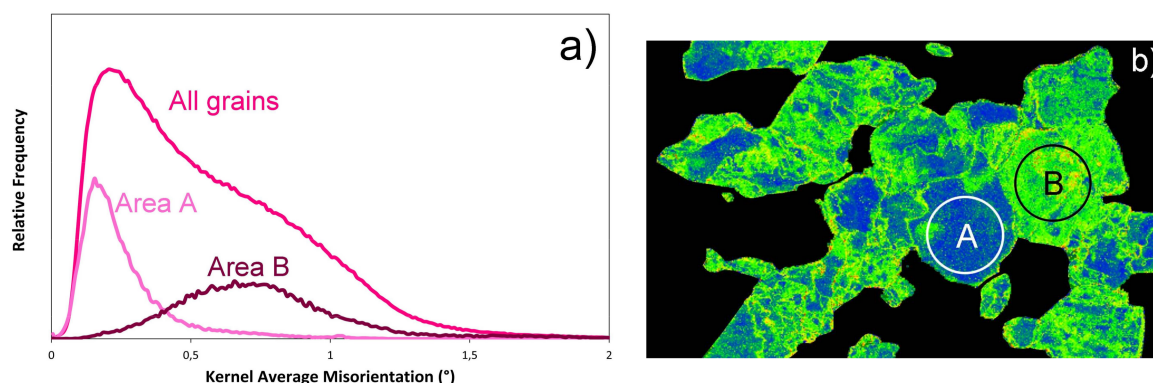


Figure 5. (a) KAM distributions (3rd nearest-neighbor) in two subsets A and B located on the KAM map (b) extracted from Figure 2e.

5. Conclusions

As previously shown with bridgmanite and ferropericlase [14], we present here a new demonstration that SPED is well adapted to the study of plastic deformation of mantle phases deformed at high-pressure and high-temperature. This is made possible thanks to the short acquisition time at each probe location which preserves beam-sensitive phases. The spot patterns of SPED are also very robust against highly deformed materials, and the technique is well suited to characterize highly deformed phases with dislocation densities which become challenging for standard weak-beam dark-field characterizations. Hence, we suggest that SPED represents an interesting means of studying samples deformed at high-pressure, even without coupling with a synchrotron beamline. Considering the limited availability of synchrotron access, this might open interesting perspectives for high-pressure deformation facilities. Moreover, we show here that even for studies carried out at the synchrotron, SPED can provide complementary information.

In the present case, where the plastic behavior of wadsleyite and ringwoodite at 17.3 GPa, 1700 K was studied, we find no significant contrast in the plastic response of both phases, except that recovery by subgrain boundary migration seems to be more easily activated in wadsleyite.

Acknowledgments: This work was supported by funding from the European Research Council under the Seventh Framework Programme (FP7), ERC grant No. 290424—RheoMan to P. Cordier. The TEM facility in Lille (France) is supported by the Conseil Régional du Nord-Pas de Calais, and the European Regional Development Fund (ERDF). The deformation experiment was supported by the power user program of SPring-8. We acknowledge the DFG for funding of the FIB facility in Bayreuth (grant INST 91/315-1 FUGG).

Author Contributions: P.C. and A.M. conceived the study; T.K. performed the experiments; B.C.N., S.T., A.M., P.C. and N.M. performed TEM studies; S.T. analyzed the data with B.C.N. and J.B.; All authors discussed and interpreted the results. P.C. wrote the paper with contributions of all authors.

Conflicts of Interest: The authors declare no conflict of interest. The founding sponsors had no role in the design of the study; in the collection, analyses, or interpretation of data; in the writing of the manuscript, and in the decision to publish the results.

References

1. Mitrovia, J.X.; Forte, A.M. A new inference of mantle viscosity based upon joint inversion of convection and glacial isostatic adjustment data. *Earth Planet. Sci. Lett.* **2004**, *225*, 177–189. [\[CrossRef\]](#)
2. Liu, X.; Zhong, S. Constraining mantle viscosity structure for a thermochemical mantle using the geoid observation. *Geochem. Geophys. Geosyst.* **2016**, *17*, 895–913. [\[CrossRef\]](#)
3. Fukao, Y.; Obayashi, M.; Nakakuki, T.; the Deep Slab Project Group. Stagnant Slab: A Review. *Annu. Rev. Earth Planet. Sci.* **2009**, *37*, 19–46. [\[CrossRef\]](#)
4. Yamazaki, D.; Karato, S. High-pressure rotational deformation apparatus to 15 GPa. *Rev. Sci. Instrum.* **2001**, *72*, 4207. [\[CrossRef\]](#)
5. Wang, Y.; Durham, W.B.; Getting, I.C.; Weidner, D.J. The deformation-DIA: A new apparatus for high temperature triaxial deformation to pressures up to 15 GPa. *Rev. Sci. Instrum.* **2003**, *74*, 3002. [\[CrossRef\]](#)
6. Kawazoe, T.; Karato, S.-I.; Ando, J.-I.; Jing, Z.; Otsuka, K.; Hustoft, J.W. Shear deformation of polycrystalline wadsleyite up to 2100 K at 14–17 GPa using a rotational Drickamer apparatus (RDA). *J. Geophys. Res.* **2010**, *115*, B08208. [\[CrossRef\]](#)
7. Kawazoe, T.; Nishihara, Y.; Ohuchi, T.; Nishiyama, N.; Higo, Y.; Funakoshi, K.; Irifune, T. In situ stress–strain measurements in a deformation–DIA apparatus at P–T conditions of the upper part of the mantle transition zone. *Am. Mineral.* **2011**, *96*, 1665–1672. [\[CrossRef\]](#)
8. Nishiyama, N.; Wang, Y.; Uchida, T.; Irifune, T.; Rivers, M.L.; Sutton, S.R. Pressure and strain dependence of the strength of sintered polycrystalline Mg₂SiO₄ ringwoodite. *Geophys. Res. Lett.* **2005**, *32*, L04307. [\[CrossRef\]](#)
9. Miyagi, L.; Amulele, G.; Otsuka, K.; Du, Z.; Farla, R.; Karato, S.-I. Plastic anisotropy and slip systems in ringwoodite deformed to high shear strain in the Rotational Drickamer Apparatus. *Phys. Earth Planet. Inter.* **2014**, *228*, 244–253. [\[CrossRef\]](#)
10. Kawazoe, T.; Nishihara, Y.; Ohuchi, T.; Miyajima, N.; Maruyama, G.; Higod, Y.; Funakoshi, K.; Irifune, T. Creep strength of ringwoodite measured at pressure–temperature conditions of the lower part of mantle transition zone using a deformation–DIA apparatus. *Earth Planet. Sci. Lett.* **2016**, *454*, 10–19. [\[CrossRef\]](#)
11. Hughes, D.A.; Liu, Q.; Chrzan, D.C.; Hansen, N. Scaling of microstructural parameters: Misorientations of deformed induced boundaries. *Acta Mater.* **1997**, *45*, 105–112. [\[CrossRef\]](#)
12. Hughes, D.A.; Liu, Q.; Chrzan, D.C.; Hansen, N. Scaling of misorientation distributions. *Phys. Rev. Lett.* **1998**, *81*, 4664–4667. [\[CrossRef\]](#)
13. Ghamarian, I.; Liu, Y.; Samimi, P.; Collins, P.C. Development and application of a novel precession electron diffraction technique to quantify and map deformation structures in highly deformed materials—As applied to ultrafine-grained titanium. *Acta Mater.* **2014**, *79*, 203–215. [\[CrossRef\]](#)
14. Nzogang, B.C.; Bouquerel, J.; Cordier, P.; Mussi, A.; Girard, J.; Karato, S. Characterization by scanning precession electron diffraction of an aggregate of bridgmanite and ferropericlae deformed at HP-HT. *Geochem. Geophys. Geosyst.* **2018**, *19*. [\[CrossRef\]](#)
15. Rauch, E.F.; Véron, M. Automated crystal orientation and phase mapping in TEM. *Mater. Charact.* **2014**, *98*, 1–9. [\[CrossRef\]](#)
16. Horiuchi, H.; Sawamoto, H. Beta-Mg₂SiO₄: Single-crystal X-ray diffraction study. *Am. Mineral.* **1981**, *66*, 568–575.
17. Hazen, R.M.; Downs, R.T.; Finger, L.W. Crystal chemistry of ferromagnesian silicate spinels: Evidence for Mg–Si disorder. *Am. Mineral.* **1993**, *78*, 1320–1323.
18. Rauch, E.F.; Dupuy, L. Rapid spot diffraction patterns identification through template matching. *Arch. Metal. Mater.* **2005**, *50*, 87–99.
19. Wright, S.I.; Nowell, M.M.; Field, D.P. A review of strain analysis using electron backscatter diffraction. *Microsc. Microanal.* **2011**, *17*, 316–329. [\[CrossRef\]](#) [\[PubMed\]](#)
20. Godfrey, A.; Cao, W.Q.; Liu, Q.; Hansen, N. Stored energy, microstructure, and flow stress of deformed metals. *Metal. Mater. Trans. A* **2005**, *36*, 2371–2378. [\[CrossRef\]](#)
21. Barbe, F.; Forest, S.; Cailletaud, G. Intergranular and intragranular behavior of polycrystalline aggregates. Part 2: Results. *Int. J. Plast.* **2001**, *17*, 537–563. [\[CrossRef\]](#)
22. Ham, R.K. The determination of dislocation densities in thin films. *Philos. Mag.* **1961**, *6*, 1183–1184. [\[CrossRef\]](#)
23. Littlewood, P.D.; Wilkinson, A.J. Geometrically necessary dislocation density distributions in cyclically deformed Ti–6Al–4V. *Acta Mater.* **2012**, *201260*, 5516–5525. [\[CrossRef\]](#)

24. Zhu, C.; Harrington, T.; Livescu, V.; Gray, G.T., III; Vecchio, K.S. Determination of geometrically necessary dislocations in large shear strain localization in aluminum. *Acta Mater.* **2016**, *118*, e383–e394. [[CrossRef](#)]
25. Rottmann, P.F.; Hemker, K.J. Nanoscale elastic strain mapping of polycrystalline materials. *Mater. Res. Lett.* **2018**, *6*, 249–254. [[CrossRef](#)]
26. Rollett, A.D.; Wagner, F.; Allain-Bonasso, N.; Field, D.P.; Lebensohn, R.A. Comparison of Gradients in Orientation and Stress between Experiment and Simulation. *Mater. Sci. Forum* **2012**, *702*, 463–468. [[CrossRef](#)]



© 2018 by the authors. Licensee MDPI, Basel, Switzerland. This article is an open access article distributed under the terms and conditions of the Creative Commons Attribution (CC BY) license (<http://creativecommons.org/licenses/by/4.0/>).